THE JOURNAL OF PHYSICAL CHEMISTRY C
A JOURNAL OF THE AMERICAN CHEMICAL SOCIETY

pubs.acs.org/JPCC

Article

Kinetic Monte Carlo Approach as a Tool for the Study of Magnetic Hyperthermia Efficiency

C. M. Aono, V. R. R. Aquino, A. F. Bakuzis, and R. Miotto*

Cite This: *J. Phys. Chem. C* 2025, 129, 927−939

ABSTRACT: This study focuses on the development and implementation of a computational model based on a two-level system framework, employing a kinetic Monte Carlo approach, to simulate the behavior of magnetic nanoparticles in fluid environments under alternating magnetic field excitation. The primary goal is to develop a tool to be used in the investigation of the impact of different nanoparticle properties on the efficiency of magnetic hyperthermia. A crucial aspect of this investigation is the rigorous validation of the computational model through comprehensive comparisons with experimental observations varying particle size, concentration, and magnetic field amplitude and frequency, ensuring the reliability and accuracy of the model in capturing the complex dynamics of nanoparticles in suspension and its influence on hyperthermia efficiency. Our findings underscore the potential of this computational model as a predictive tool for estimating Specific Loss Power (SLP) metrics across various systems subjected to different applied magnetic fields. By delineating the relationship between the nanoparticle's characteristics and hyperthermia efficiency, this study contributes to advancing the fundamental understanding and predictive capabilities of magnetic nanoparticle-based hyperthermia therapies.

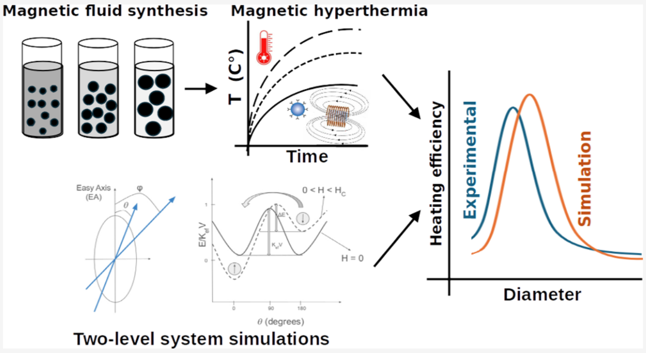

INTRODUCTION

This work explores the field of healthcare-focused nanotechnologies, encompassing a broad spectrum commonly referred to as nanomedicine. Within this research area, applications are diverse and include the utilization of nanostructures, such as nanocarriers for drug delivery, advanced imaging and diagnostic techniques, and the development of biomaterials tailored for prosthetic applications, among others.[1]

In this study, theoretical methodologies rooted in nanomagnetism and computational simulations are harnessed to scrutinize the dynamics of the nanoparticle magnetic moments. Nanomagnetism, a field of study, extends its applications from the investigation of magnetic evolution for sample dating purposes[2] to the innovation and construction of high-density hard disks (HD) for information storage.[3]

Within the domain of medical physics, magnetic nanoparticles (MNPs) find versatile applications, including drug transportation mechanisms,[4−7] magnetic separators,[8] and serve as contrast agents for MRI[9,10] or magnetic tracers, notably in tomography, such as magnetic particle imaging (MPI).[11,12] MNPs have a key part in a treatment modality known as magnetic hyperthermia (MH),[13] which is the central focus of this research paper.

Hyperthermia, a long-standing medical technique, is employed to induce cellular death by raising temperatures in specific regions for a given period of time during the therapeutic procedure. In the context of neoplasms, this thermal elevation operates in two ways: temperatures between 41 and 46 °C trigger alterations in intracellular protein expression and functionalities, gradually instigating cellular degradation and eventual apoptosis (programmed cell death). Therefore, within these temperature thresholds, treatment is often combined with radiotherapy or chemotherapy. Beyond 46 °C, direct cellular death occurs.[14]

Hyperthermia as a neoplasm treatment aligns with modern methodologies, presenting viable alternatives to traditional approaches, such as surgery, radiotherapy, and chemotherapy. Modern strategies aim to amalgamate two pivotal aspects distinguishing them from conventional methodologies: selectivity (targeting solely diseased cells) and efficiency (expediting the demise of diseased cells with diminished side effects). Hyperthermia is also a promising candidate for heat-induced cancer immunotherapy.[15]

Magnetic hyperthermia involves the administration of magnetic nanoparticles into the patient, in general, intra-

Received: October 20, 2024
Revised: December 6, 2024
Accepted: December 9, 2024
Published: December 26, 2024

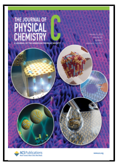

https://doi.org/10.1021/acs.jpcc.4c07127
J. Phys. Chem. C 2025, 129, 927−939

tumoral, (although systemic administration is also under investigation with new nanotechnology-based strategies, like cell-membrane coating[10]), followed by the application of a radio frequency magnetic field (100−300 kHz).[13] This interaction between the magnetic field and magnetic moment of the MNPs precipitates the release of energy in the form of heat if magnetic hysteresis is established. The genesis of this technique traces back to the seminal work of Gilchrist et al.[16] in the 1950s, which postulated the use of magnetic materials to induce localized temperature increases through radio frequency magnetic field applications.

Magnetic hyperthermia (MH) stands out as a promising approach for combating neoplasms, primarily due to the utilization of magnetic nanoparticles (MNPs) to induce controlled heat generation. MNPs, often derived from ferrites like magnetite Fe_3O_4, exhibit distinct characteristics that make them the preferred choice for MH applications.[17−20]

The efficacy of MH has been validated in numerous in vivo studies targeting neoplasms in diverse anatomical locations, including the lungs, breasts, prostate, head and neck, pancreas, and liver. Notably, MH has shown promising outcomes in addressing highly aggressive tumors such as glioblastoma.[17,21,22]

These characteristics collectively underscore the potential of MNPs in MH as a versatile and effective modality in cancer therapy. Nevertheless, further research is imperative to optimize MNP design, develop standardized protocols, and elucidate long-term safety profiles to ensure their clinical translation and widespread therapeutic application.

In the realm of magnetic fluid solutions, nanoparticles' efficacy on magnetic hyperthermia is influenced by different characteristics, such as size, concentration, and distribution. However, empirically addressing this phenomenon poses challenges due to the intricate nature of solutions presenting varying types and properties. This complexity prompts the necessity for computational simulations to systematically investigate the diverse forms and sizes of MNPs with a view to contributing to the development and design of more efficient nanoparticles for MH use.

As such, the principal objective of this study revolves around the development and implementation of a computational tool based on a two-level system model employing a kinetic Monte Carlo approach. This computational framework aims to simulate the behavior of magnetic nanoparticles within fluid environments, specifically elucidating the impact of different nanoparticle sizes and concentrations on the overall efficiency of magnetic hyperthermia. This approach has been successfully used by other groups[23−26] to investigate heat production in MNPs.

A critical facet of our investigation involves the rigorous validation of this computational model. This validation process entails a comprehensive comparison of simulations with experimental observations. By rigorously aligning computational predictions with empirical findings, we strive to establish the reliability and accuracy of our computational approach in capturing the complex dynamics of nanoparticles in suspension and their influence on magnetic hyperthermia efficiency.

Importantly, our findings underscore the potential of this computational model to serve as a predictive tool for estimating efficiency metrics, particularly specific loss power (SLP), across a spectrum of systems subjected to varying applied magnetic fields. By delineating the relationship between nanoparticle characteristics in suspension and hyperthermia efficiency, our study contributes to advancing the fundamental understanding and predictive capabilities in the realm of magnetic nanoparticle-based hyperthermia therapies. In this study, we focus on Mn-doped iron oxide nanoparticles, specifically, Mn-ferrite nanoparticles. This material closely resembles magnetite but with Mn^{2+} ions replacing Fe^{2+}. This substitution impacts the magnetization and magnetic anisotropy of the nanoparticles. The resulting softer magnetic nanomagnets exhibit promising applications in low-field magnetic hyperthermia, alternating current biosusceptometry, and magnetic resonance imaging.[10,27−29]

Our work is organized as follows: first, we discuss the synthesis and characterization of the $MnFe_2O_4$ particles and the theoretical modeling, technical details, and limitations of our proposed implementation. Next, we directly compare our simulated results with experimental data obtained in our group to validate our approach. Finally, we demonstrate that our model can be used to estimate the specific loss power (SLP) across various systems subjected to different applied magnetic fields.

■ METHODS

Synthesis of $MnFe_2O_4$. The iron oxide-based particles/magnetic fluid were synthesized in a two-step process. First, the nanoparticles ($MnFe_2O_4$) were prepared following the procedure reported by Aquino et al.[30,31] In a typical experiment, a solution of $FeCl_3·6H_2O$ and $MnCl_2·6H_2O$ was mixed with different bases. For small sizes, we used 40 wt % methylamine (CH_3NH_2); for medium diameters, 28 wt % ammonium hydroxide (NH_4OH); and for larger sizes, sodium hydroxide (NaOH). To suspend the nanoparticles in water, we used trisodium citrate dihydrate ($Na_3C_6H_5O_7·2H_2O$), obtaining colloidal dispersions of magnetic particles in a carrier liquid.

Samples with different sizes and low polydispersity were obtained from a mother sample using the method of diameter separation by ionic strength.[32] This method induces a phase transition through changes in colloidal forces, leading to the segregation of the nanoparticles. NaCl was added to the medium, affecting colloidal stability and causing a gas−liquid transition, resulting in two phases: one with more dispersed nanoparticles of smaller diameters (gas type) and the other with larger, more concentrated nanoparticles (liquid type). Additionally, magnetic separation was performed by placing a magnet at the bottom and separating the supernatant from the sample at the bottom. Thus, samples with different average sizes and reduced polydispersities were obtained. Immediately after separation, the samples were washed three times with acetone to resuspend them. This procedure was repeated for the three mother samples synthesized with different bases: Mn2 (produced with CH_3NH_2) from which samples Mn1 and Mn3 were obtained, Mn5 (produced with NH_4OH) from which samples Mn4 and Mn6 were obtained, and Mn8 (produced with NaOH) from which samples Mn7 and Mn9 were obtained.

Magnetic Nanoparticle Characterization. The crystal structure of the nanoparticles was characterized using powder X-ray diffraction (XRD) experiments conducted on a Shimadzu 6000 (Cu Kα radiation) in the 2θ range of 25−65°. The morphology of the nanoparticles was characterized with a JEOL model JEM-2100 transmission electron microscope (TEM) operating at 200 kV, by measuring low-resolution and high-resolution TEM images. Hydrodynamic

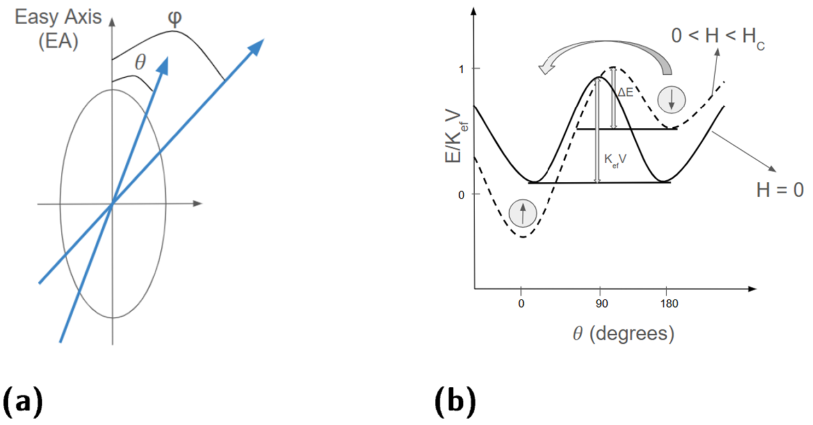

Figure 1. (a) Angle between the anisotropy axis and the magnetic moment, θ, and angle between the anisotropy axis and the magnetic field, ϕ. (b) NP energy profile with and without an external magnetic field.

diameter measurements were obtained using dynamic light scattering (DLS) with a Zetasizer Nano S ZEN 1600 model from Malvern. Magnetic hysteresis loops were measured using a vibrating sample magnetometer (VSM) (ADE Magnetic, Model EV-9) operating in the range of ±20 kOe at room temperature. Additionally, magnetohyperthermia (MH) measurements were performed in an oscillating magnetic field with frequencies ranging from 174 to 988 kHz using Nanotherics equipment, model magneTherm.

Theoretical Modeling. Heat generation in magnetic materials for magnetic hyperthermia arises through hysteresis loss.[14,31,33,34] Hysteresis can happen through nonfrequency or frequency-dependent loss. Larger particles, such as noparticles in the quasi-static blocked regime, show hysteresis. This can arise from single-domain nanoparticles at the blocked regime or through domain wall movements in multidomain nanoparticles. Smaller nanoparticles, that are superparamagnetic at quasi-static (DC) field conditions, and single-domain, also can release heat when excited by AC magnetic fields, a phenomenon known as dynamic hysteresis.[23,31,35] In this case, heat can arise through Néel or Brown relaxation processes. Néel relaxation arises from internal magnetic moment rotations inside the nanoparticle without the particle itself rotating, while Brownian relaxation results from the rotation of the nanoparticle in the liquid medium as a result of the magnetic excitation. So, heat release is related to the spin-phonon interaction in Néel relaxation, while for Brownian relaxation it arises from the friction with the liquid carrier under an oscillating magnetic field.

The Rosensweig model[36] is a linear response theory that takes into account these relaxations, focusing on noninteracting, evenly dispersed, and single-domain MNPs. In this scheme, the power released obtained from the hysteresis loss can be expressed as[14]

$$P = \frac{1}{2}\omega\mu_0\chi_0 H^2 \frac{\omega\tau}{1+\omega^2\tau^2} \tag{1}$$

where P is the power dissipated per unit of volume; H is the external magnetic field, ω is the frequency of oscillations of the external magnetic field, μ_0 is the vacuum permeability, χ_0 is the magnetic susceptibility of the sample, and τ is the relaxation time of the macrospins.

In this approximation, the modified Néel,[14,37] Brown, and total relaxation times can be expressed as

$$\tau_N = \frac{\tau_0}{2}\sqrt{\pi\frac{k_B T}{KV}}\, e^{KV/k_B T} \tag{2}$$

$$\tau_B = \frac{3\eta V_H}{k_B T} \tag{3}$$

and

$$\frac{1}{\tau} = \frac{1}{\tau_B} + \frac{1}{\tau_N} \tag{4}$$

where τ_N, τ_B, and τ are the Néel, Brown, and total relaxation times, τ_0 is a time constant, k_B is the Boltzmann constant, K is the anisotropy constant, T is the temperature, V is the particle volume, η is the liquid viscosity, and V_H is the particle's hydrodynamic volume.

Since Rosensweig's model is a linear response theory, only elliptical hysteresis curves are achieved, which are only valid at the low field regime, as pointed out by Carrey et al.[23] Indeed, due to the formation of clusters and interactions among the NPs, both relaxation effects might occur simultaneously. In this sense, models that are able to take into account nonlinear responses are necessary to adequately simulate MH at higher field amplitude.

From a theoretical perspective, Tan et al.[24] introduced a quantity that measures this efficiency in the case of heat dissipation through hysteresis, which depends on the normalized hysteresis curve area (A), the frequency of external magnetic field oscillation (f), the saturation magnetization of the sample (M_S), and the simulated magnetic fluid density (ρ):

$$\mathrm{SLP} = \frac{A \times f \times M_s}{\rho} \tag{5}$$

From the experimental point of view, the corresponding quantity is named either specific loss power (SLP) or specific absorption rate (SAR). In the following discussions, for simplicity, we will address both the theoretical and experimental quantities as SLP.

Hence, simulating magnetic dynamics through stochastic methods will enable us to obtain hysteresis curves, compare simulated and experimental SLP values for different MNP conditions, and subsequently study the optimization of parameters for magnetic hyperthermia.

Two-Level System Approximation. In this study, an alternative methodology based on a two-level model is employed to overcome the inherent limitations associated

https://doi.org/10.1021/acs.jpcc.4c07127
J. Phys. Chem. C 2025, 129, 927−939

with directly integrating the Landau-Lifshitz−Gilbert equation, which is usually used to simulate isolated nanoparticles. When examining theoretical models for investigating single-domain nanoparticles (NPs), those derived from the two-level model emerge as the most suitable candidates for studying an ensemble of Magnetic Nanoparticles (MNPs) intended for application in magneto-hyperthermia. Unlike models relying on equilibrium functions (Langevin functions) or linear response theory (LRT), these models exhibit the capability to effectively characterize NPs under nonlinear response conditions.[23]

The Stoner and Wohlfarth model,[38] introduced in 1948 to elucidate the magnetic hysteresis of single-domain particles, adopts a macrospin approximation, which becomes particularly pertinent for nanoparticles (NPs) at the size range used in MH.[39] This model offers a framework to describe the energy of a single-domain nanoparticle exhibiting uniaxial anisotropy, as expressed in eq 6

$$E = \underbrace{K_{ef}V\,\mathrm{sen}^2(\theta)}_{\text{anis}} - \underbrace{\mu_0\mu H_{tot}\cos(\phi - \theta)}_{\text{field}} \tag{6}$$

where K_{ef} is the effective magnetic anisotropy constant, V the NP volume, μ_0 the magnetic permeability, μ the NP magnetic moment, H_{tot} the effective magnetic field, θ the angle between the anisotropy axis and the magnetic moment, ϕ the angle between the anisotropy axis and the magnetic field. θ and ϕ are represented in Figure 1a, for the sake of clarity. In eq 6, the indexes anis and field indicate the magnetic anisotropy and applied magnetic and dipolar field contributions, respectively.

In this study, the interaction among magnetic nanoparticles (MNPs) plays a central role in the analyses conducted. Within eq 6, H_{tot} can be written as a combination of several terms. Tan et al.[24] propose that the total field can be written as a combination of an applied external field ($\mu_0\overrightarrow{H_{ext}}$) and a contribution from the dipolar interaction ($\mu_0\overrightarrow{H_{dip}}$), which depends on the relative positions between the MNPs. These terms can be written as

$$\mu_0\overrightarrow{H_{ext}} = A \times \cos(2\pi \times f \times t) \tag{7}$$

$$\mu_0\overrightarrow{H_{dip}} = \frac{\mu_0 M_S V}{4\pi}\sum_{i\neq j}\frac{3(\overrightarrow{m_j}\times\overrightarrow{e_{ij}})\overrightarrow{e_{ij}} - \overrightarrow{m_j}}{r_{ij}^3} \tag{8}$$

where A and f are the amplitude and frequency of the external field, respectively, and t is the simulation time. Additionally, M_s denotes the saturation magnetization, $\overrightarrow{m_j}$ represents the magnetic moment of particle j, rij is the distance between the ith and jth particles, and $\overrightarrow{e_{ij}}$ is the unit vector in the direction of r_{ij}.

An important limitation of the Stoner−Wohlfarth model lies in its failure to account for thermal activation within the system. To overcome this limitation and extend the model to encompass more complex systems, one approach involves introducing thermal activation, approximating it through a two-level system.[23] To achieve this, it becomes necessary to normalize eq 6 with respect to k_BT:

$$\frac{E(\theta, \phi)}{k_BT} = \sigma\sin^2(\theta) - \xi\cos(\theta - \phi) \tag{9}$$

where:

$$\sigma = \frac{K_{ef}V}{k_BT} \tag{10a}$$

$$\xi = \frac{\mu_0\mu H_{tot}}{k_BT} \tag{10b}$$

The energy profile for the case of $H_{ext} = 0$ exhibits two energy minima of equal magnitude (see Figure 1b). However, under the influence of an external magnetic field, there is an imbalance among these energy levels. In particular, the formation of two minima occurs when the anisotropy field ($\mu_0H_K = 2K_{eff}/M_S$) exceeds μ_0H_{max}. This specific condition holds significant relevance in magnetic hyperthermia, as the transition between these states is accountable for the heat release via hysteresis phenomenon, considering an ensemble of NPs, as detailed in the study by Carrey et al.[23]

Since the behavior of eq 9 in the relevant conditions for magnetic hyperthermia presents two energy minima, the challenge regarding the magnetic dynamic response of these MNPs can be effectively conceptualized as a two-level problem. The fundamental equation governing the behavior of uniaxial magnetic nanoparticle systems with two levels is articulated as per the research by Klik et al.[40] and Chantrell et al.[41]:

$$\frac{dn_1}{dt} = \frac{n_2}{\tau_{21}} - \frac{n_1}{\tau_{12}} \tag{11}$$

where n_1 is the number of particles in energy state 1; n_2 is the number of particles in energy state 2; τ_{21} is the relaxation time from level 2 to level 1; and τ_{12} is the Relaxation time from level 1 to level 2.

In terms of probability, eq 11 can be rewritten as

$$\frac{dP_1}{dt} = \frac{P_2}{\tau_{21}} - \frac{P_1}{\tau_{12}} = \frac{1 - P_1}{\tau_{21}} - \frac{P_1}{\tau_{12}} \tag{12}$$

where $P_1(t)$ − Probability of transition from energy state 2 to 1 after time t; $P_2(t)$ − Probability of transition from energy state 1 to 2 after time t.

The equation above represents a separable differential equation, which can be integrated, considering the initial condition $P_1(0) = 0$, to find an expression for $P_1(t)$:

$$P_1(t) = \frac{\tau_{21}^{-1}}{\tau^{-1}} - \frac{\tau_{21}^{-1}}{\tau^{-1}} \times \mathrm{e}^{-t/\tau} \tag{13}$$

It is more convenient to express eq 13 in terms of transition frequencies between energy levels.

$$P_1(t) = \frac{\nu_2}{\nu_1 + \nu_2} \times [1 - \mathrm{e}^{-t\times(\nu_1+\nu_2)}] \tag{14}$$

where $\tau_{21} = \frac{1}{\nu_2}$; $\tau_{12} = \frac{1}{\nu_1}$; $\tau^{-1} = \nu_1 + \nu_2$.

Equation 14 is written in terms of ν_1 and ν_2, which are the transition frequencies from states 1 to 2 and 2 to 1, respectively. With a comprehensive description of the energy barrier between the two levels and the transition probability between them, it is feasible to implement an algorithm based on the kinetic Monte Carlo method (kMC) that will be detailed ahead. Through this stochastic method, it is possible to obtain hysteresis curves for different configurations of MNPs.

Limitations of the Model. The macrospin approximation assumes that all of the atomic magnetic moments in a nanoparticle rotate uniformly, treating the entire nanoparticle as a single magnetic domain with a collective magnetic moment. While this approximation simplifies the description of magnetic behavior, especially in theoretical models like the Stoner−Wohlfarth model,[38] it has several limitations when describing the magnetic properties of a magnetic nanoparticle. For very small nanoparticles (typically below a few nanometers), the macrospin approximation can be valid because thermal fluctuations dominate and the particle tends to behave as a single magnetic domain. However, for larger particles, multidomain states can form where different regions of the nanoparticle have distinct magnetic moments, breaking the uniformity assumed in the macrospin model.[42]

In addition, nanoparticles are often packed closely together, leading to interactions between their magnetic moments (dipole−dipole interactions and exchange coupling). The macrospin approximation does not account for these interparticle interactions, which can affect the overall magnetic behavior of the system.[42] The macrospin model does not adequately capture the effects of thermal fluctuations at higher temperatures. In small nanoparticles, thermal energy can induce random fluctuations of the magnetic moment, leading to superparamagnetism.[43−45]

The macrospin approximation also neglects surface effects, assuming uniform magnetization throughout the particle, while in nanoparticles, the surface atoms often have different magnetic properties than the atoms in the core (e.g., due to broken symmetry, surface anisotropy, or different bonding environments).[46] In a similar manner, anisotropy variations are not taken into consideration since the macrospin approximation assumes a single, uniform anisotropy direction (often uniaxial). However, nanoparticles can exhibit complex anisotropy landscapes due to shape irregularities, crystalline defects, and surface anisotropy. These variations can lead to nonuniform magnetization behavior, not captured by the approximation.[47]

The macrospin model is inherently classical, and it fails to account for quantum mechanical effects such as quantum tunneling of magnetization (important in smaller particles at low temperatures and hence irrelevant for magnetic hyperthermia). These effects can lead to magnetic behavior that deviates significantly from classical predictions.[48] It also assumes a rigid rotation of the magnetic moment, ignoring the internal dynamics of individual spins within the nanoparticle. In reality, individual atomic spins may respond differently to external fields or interactions, leading to noncoherent spin dynamics that are not accounted for in the macrospin approach.[49]

While the Stoner−Wolfarth model aims to obtain the lowest energy configuration for the magnetization, that is, it is based on the minimization of energy with respect to the angle between the magnetization and the anisotropy axis, the implemented two-level system approximation makes use of a stochastic approach, i. e. an ensemble of different configurations are considered and the derived properties are obtained from an average behavior of the system.

Monte Carlo simulations are not inherently time-dependent. While the algorithm provides a statistical average over configurations, it does not model the time evolution of the system but provides an approximation of real-time dynamics.[50] Since Monte Carlo is a stochastic method, results will exhibit statistical noise due to the random sampling process. To reduce this noise and obtain accurate averages, many independent simulations or long runs are necessary, which increase computational cost. The level of noise can vary based on the system's complexity and the number of Monte Carlo steps.[51] Examples of noise-derived deviations for our target systems can be seen in the center of the hysteresis loop presented in Figure S3 of the Supporting Information.

In the present simulation, since we are considering the magnetic moment of each NP as a macrospin, the single-particle hysteresis contribution is not explicitly taken into account. The hysteresis will arise from the ensemble of magnetic NPs. As a result, one might expect that the simulated and experimental SLP values should not necessarily be in the same order. However, since the NP arrangement and dipolar interaction are explicitly taken into consideration, the overall behavior of the experimental and simulated SLP are expected to follow similar patterns.

In summary, while the macrospin approximation is useful for small, isolated nanoparticles at low temperatures, it becomes less accurate when dealing with larger particles, interactions between particles, surface effects, and thermal or quantum fluctuations. Our Monte Carlo implementation is not inherently time-dependent and exhibits statistical noise due to the random sampling process.

Kinetic Monte Carlo Implementation. Having established that eq 14 describes the magnetic dynamics of a specific ensemble of Magnetic Nanoparticles (MNPs) within a two-level system, the next phase of our research involves developing a Kinetic Monte Carlo algorithm. It is worth noting that this approach has been successfully applied by other research groups, including Papadopoulos et al.[26] and Ruta et al.[25] In both studies, Kinetic Monte Carlo approximations were used to investigate how various parameters, such as frequency, particle size, anisotropy constants, MNP shape, and distribution, affect heat production. However, a direct comparison between our results and those of Papadopoulos et al.[26] and Ruta et al.[25] is not feasible, as essential details of their studies, such as the number of nanoparticles considered and initial configurations, are not available.

Additionally, it is important to highlight that our approach differs fundamentally from previous studies, such as those by Papadopoulos et al.[26] and Ruta et al.[25] While these works primarily aim to explore how nanoparticle properties—such as magnetization, size, volume, and anisotropy constant—affect the specific loss power (SLP) response, our approach uses experimentally measured values as input parameters. This enables us to directly compare simulated results with experimental data rather than focusing on identifying the set of input parameters that best fit the experimental observations numerically.

During the dynamics, the magnetic moment of a nanoparticle visits multiple configurations, and this system can be studied using stochastic theory, namely, Monte Carlo methods. Specifically, we will employ a Kinetic Monte Carlo algorithm inspired by references.[23,24]

Magnetic Fluid Initial Conditions. A key point in simulating the magnetic dynamics of the Magnetic Nanoparticles (MNPs) ensemble lies in establishing the initial conditions of the system. To accurately describe the positions and magnetic moments of our MNP ensemble, we utilized the implementation proposed by Castro and colleagues,[52] as detailed by Bakuzis,[53] who also makes use of a Monte Carlo approach. In order to avoid confusion, we will refer to Castro's

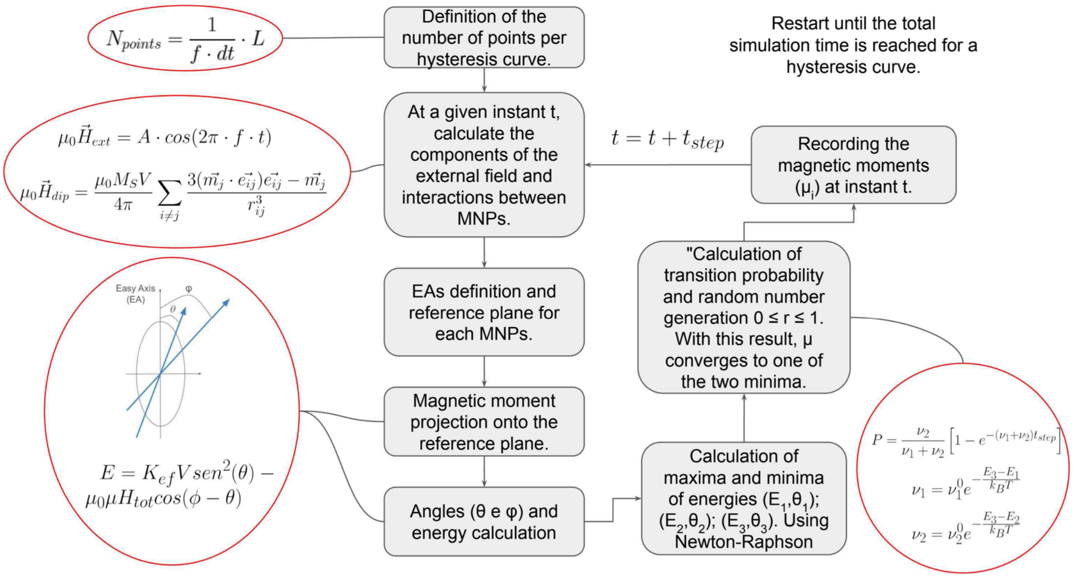

Figure 2. Schematic representation of the magnetic dynamics algorithm for MNPs using Kinetic Monte Carlo.

approach simply as *magnetic fluid initial conditions Monte Carlo simulations* or MFIC for short. Briefly, within each Monte Carlo step (MC step) on MFIC, the configuration of a given nanoparticle undergoes random changes in both position and magnetic moment to generate a new configuration.

The overall interaction potential (U_{total}) between a pair of ionic-surfaced magnetic nanoparticles (indexed as i and j) is computed by summing individual terms across all considered pairs, as expressed in eq 15:

$$U_{\text{total}}(ij) = U_{\text{m}}(ij) + U_{\text{w}}(ij) + U_{\text{s}}(ij) + U_{i}(ij) + U_{\text{B}}(ij) \tag{15}$$

where U_{m} represents the magnetic dipolar interaction, U_{w} signifies the van der Waals interaction, U_{s} denotes steric repulsion, U_i refers to ionic repulsion, and U_{B} accounts for the Zeeman interaction.

As extensively described in a prior study,[52] the MFIC implementation begins with a random configuration of the considered nanoparticles, subject to the interactions delineated in eq 15. It then proceeds by executing successive minor variations in all nanoparticle coordinates. In the simulated magnetic fluid system investigated in this study, a configuration is defined by the nanoparticles' positions and the orientations of their magnetic dipole moments. Consequently, within each iteration of the Metropolis algorithm, both the positions and orientations of the magnetic dipole moments of all considered nanoparticles undergo random changes. Each simulation involved a minimum of 400 nanoparticles confined within a cubic box with sides measuring around 300 nm. Details of these simulations can be found in the Supporting Information (SI), Section S3.

Kinetic Monte Carlo Implementation Technical Details. In our algorithm, we construct the magnetic hysteresis curve based on the positions of magnetic nanoparticles (MNPs) and the average diameter of each MNP, following a specific setup of magnetic dynamics. A detailed discussion of these aspects is provided below and in Section S4, Simulation's technical details, of the Supporting Information (S.I.).

In the initial phase of our implementation, we determined the number of points for each hysteresis curve (N_{points}). Once the input sets are defined, the algorithm sets the magnetization easy axis for each nanoparticle, projects, and normalizes the magnetic moment. We calculate angles θ and ϕ to evaluate the energy using external and dipolar magnetic fields. Energy extrema are found, and transition probabilities are computed considering thermal activation. A random number determines state transitions, repeated for each nanoparticle. Total magnetization is summed, and an average over the cycles generates a single hysteresis curve. Multiple loops are averaged to account for variations. Figure 2 illustrates a flowchart of the aforementioned algorithm that is detailed described in Section S4, Simulation's technical details, of the Supporting Information.

As described in Supporting Information (S4), Simulation's technical details, transition frequencies are dependent on the total energy profile of the magnetic nanoparticles (MNPs), which, in turn, is connected to the angles between the easy axis of magnetization and both the external field (ϕ) and the magnetic moment (θ). Consequently, the behavior of the easy axis of magnetization is observed to be a pivotal factor. Hence, two options for the easy axis behavior were incorporated: fixed-position easy axes and dynamically changing easy axes with each step of the dynamics. In the case of dynamically shifting easy axes, the model can be interpreted as simulating both Néel and Brownian relaxations concurrently.[24] For the simulations presented in this study, the external magnetic field is consistently oriented along the z-axis, while the dynamic easy axes undergo alterations at each time step for each MNP.

In order to illustrate how hysteresis loops are constructed following our Kinetic Monte Carlo implementation, in Figure SI-S3, a hysteresis loop of a standard configuration constructed with just 60 nanoparticles is presented.

■ RESULTS AND DISCUSSION

Experimental Characterization. The TEM micrographs in Figure 3a−c display a collection of nanoparticles (NPs) synthesized using CH_3NH_2, NH_4OH, and NaOH, clearly providing different mean size distributions. In the inset, interplanar distances are observed, highlighting the high crystallinity of the material's structure. The size histograms

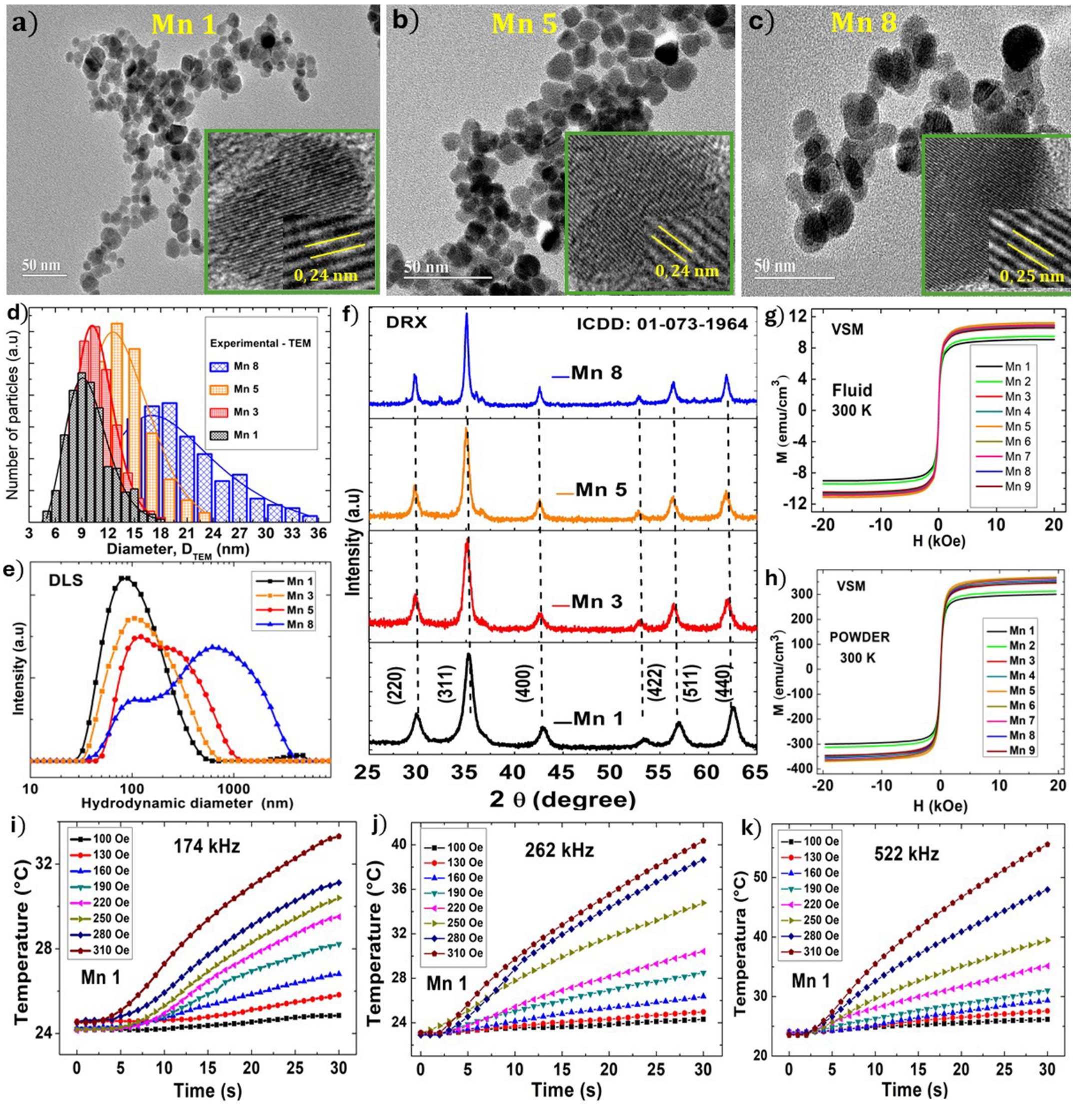

Figure 3. (a,b) General size distribution for Mn1, Mn5, and Mn8 obtained from the TEM with a scale bar of 50 nm. In inset, the high-resolution TEM. (d,e) shows the size distribution of NPs obtained from particle counting from TEM images and provides the hydrodynamic sizes of Mn1, Mn3, Mn5, and Mn8 NPs. (f) X-ray powder diffraction (XRD) identified a single crystalline phase on the samples. (g,h) hysteresis curves of the magnetic powder and fluid samples. (i–k) Magnetic hyperthermia, showing temperature versus time of at a concentration of 3% in different frequencies and magnetic field amplitudes.

Table 1. Characterization Parameters Obtained using XRD, TEM, VSM, and DLS Techniques for Mn1-9 Samples[a]

sample	diameter (XRD) (nm)	diameter (TEM) (nm)	dispersion	hydrodynamic diameter (nm)	saturation on magnetic powder (emu/g)	saturation on magnetic fluid (emu/g)
Mn 1	10.2	10.2 (2.2)	0.21 (0.02)	110	300	9.0
Mn 2	10.7			313		9.4
Mn 3	11.3	11.2 (2.1)	0.18 (0.02)	117	345	10.4
Mn 4	12.7			352		10.6
Mn 5	13.6	14.0 (3.4)	0.24 (0.03)	143	369	11.1
Mn 6	14.2			366		10.9
Mn 7	16.4			363		10.8
Mn 8	17.2	18.0 (4.8)	0.30 (0.04)	560	355	10.6
Mn 9	18.6			346		10.4

[a] The values provided in parentheses represent the associated uncertainties.

(Figure 3d) of NPs counted in the TEM images were fitted with a log-normal distribution, providing the mean diameter of the NPs using the log-normal fitting parameters. ImageJ software was used to measure the diameters of the nanoparticles. Approximately 800 nanoparticles were included in the sample for counting and measurement. The results obtained are listed in Table 1. Data for the sample Mn3 are provided in the Supporting Information, Section S1.

Figure 3e presents DLS measurements from which the mean hydrodynamic diameter of the samples in the magnetic fluids is determined. The DLS results for the particle sizes of Mn1, Mn3, Mn5, and Mn8 indicate the mean hydrodynamic sizes, suggesting the existence of clusters of nanoparticles (NPs). As the particle size increases, the magnetic dipolar interaction becomes stronger, leading to the formation of larger aggregates. This is clearly seen by the presence of two or three distinct hydrodynamic size distributions within the same sample. For example, in the sample Mn8, size distributions of 116 and 890 nm are observed.

X-ray diffraction (XRD) values of the nanoparticles (NPs) are reported in Figure 3f, and the expected peak positions match those of the bulk $MnFe_2O_4$ material. The average crystallite sizes (Table 1) of these NPs were calculated using Scherrer's equation $D_{XRD} = \frac{\kappa\lambda}{\beta\cos\theta}$, where $\kappa = 0.9$ is a dimensionless shape factor, λ is the X-ray wavelength, β is the line broadening at half the maximum intensity, and θ is the Bragg angle, in radians. These results agree with the size distribution obtained through TEM images (additional XRD data for other samples and a brief discussion on experimental data are presented in the Supporting Information, S1).

Figure 3g,h shows the magnetic hysteresis curves of the samples in powder and fluid forms. The saturation magnetization (M_s) is used to calculate the particle volume fraction (ϕ), defined as $\phi = \frac{M_s^{\text{fluid}}}{M_s^{\text{powder}}}$, where M_s^{fluid} and M_s^{powder} are the saturation magnetizations of the fluid and the powder, respectively. All the magnetic fluids were prepared to have the same volume fraction (ϕ), equal to 3% (0.03) or 150 mg/mL.

Measurements of magnetic hyperthermia (Figure 3i−k) were performed at frequencies of 174, 262, and 522 kHz with field amplitudes up to 310 Oe. The magnetic hyperthermia experiments allowed for the determination of the specific loss power (SLP) values of the magnetic NPs by the calorimetric method using the expression $\text{SLP} = C\frac{m_f}{m_{NPs}} \times \frac{dT}{dt}$, where C is the specific heat of the sample (considered the same as water), m_f is the mass of the magnetic fluid, m_{NPs} is the total mass of magnetic NPs in the fluid, and $\frac{dT}{dt}$ is the maximum rate of temperature rise. For these measurements, 150 μL of magnetic fluid was used. Magnetic hyperthermia results for other diameters are presented in the Supporting Information, Section S2.

Magnetic Dynamics Simulations. The validation of the proposed implementation was performed through a comparative analysis of the simulation outcomes and experimental data presented in this work. We specifically chose this experimental set of data since there is a significant discrepancy between Specific Loss Power (SLP) results in the literature.[14] This is likely related to variations in sample size distribution, composition, and even the experimental determination of SLP, as discussed by Deatsch and Evans,[14] Rodrigo et al.,[54] and Ring et al.[55]

Table 2 outlines the modal diameters and dispersions of the MNPs investigated by using the proposed magnetic dynamics implementation. For all considered systems, our samples are composed of 400 nanoparticles, distributed in different rectangular boxes in order to access different concentrations. All data presented, unless stated otherwise, are obtained for a monodisperse system, i.e., with less than 0.1% of agglomerated nanoparticles, at a nanoparticle concentration of 0.50%.

Table 2. Modal Diameters (d) and Dispersions (σ) of the MNPs Investigated in This Work

d (nm)	9	10	11	12	14	16	19
σ	0.20	0.21	0.18	0.20	0.25	0.25	0.30

We have chosen to perform all calculations assuming monodisperse systems, as the inclusion of interparticle interactions introduces significant and complex effects on hysteresis, which become more pronounced in systems with aggregated particles.[25] Consequently, these complex behaviors could impact our systematic analysis of different MNP characteristics, potentially leading to unspecific or even incorrect inferences. However, recognizing that particle agglomeration is a crucial factor in MNP heating production, we plan to address this issue in future work. Other key parameters used in all simulations are the anisotropy constant[30] $K = 3.7 \times 10^3$ J/m^3, the saturation magnetization of the considered nanoparticles $M_S = 3.11 \times 10^6$ A/m, as experimentally obtained by our group,[56] and the temperature in the simulations $T = 300$ K. In addition, since our study aims to develop tools for investigating MNPs for potential use in magnetic hyperthermia, the field amplitudes span between 100 and 310 Oe, while the field frequencies range from 100 to 740 kHz.

The primary objective in this study is to determine whether changes induced in the simulated specific loss power (SLP) (eq 5) correspond to alterations in the experimental SLP data.

This task is evidently challenging. From an experimental perspective, as discussed previously, there is significant variation in the measured specific loss power (SLP) values, even for similar samples, as illustrated in Figure 4 of the work by Deatsch and Evans.[14] These differences in measured SLP values can span more than 2 orders of magnitude, and their underlying causes remain unclear.

For instance, our experimental SLP values for 10 nm magnetic nanoparticles (MNPs) at 190 Oe and 174 kHz range between 10 and 20 W/g, which are relatively low compared to other ferrites reported in the literature. Rodrigo et al.,[54] for example, reported SLP values close to 100 W/g for 16 nm MNPs at 200 Oe and 134 kHz. These discrepancies become even more pronounced under different external magnetic field conditions. It is also worth mentioning that some authors use only the iron mass content, in contrast to our methodology, where we use the mass of the whole nanoparticle. In addition, we consider the magnetic field amplitude and not the RMS value.

At this stage, we can speculate only that small variations in sample properties and in the methods used to measure SLP may result in substantial numerical differences in the experimental SLP values.

Similarly, the simulated SLP values are highly sensitive to the parameters used, particularly the saturation magnetization (M_s), anisotropy constant (K), the diameter, and packing of the MNPs, as well as the amplitude and frequency of the external magnetic field. While prior works, such as those by Papadopoulos et al.[26] and Ruta et al.,[25] primarily focus on identifying the combinations of M_s, K, external magnetic field parameters, and MNP characteristics that maximize simulated SLP, our approach uses experimentally measured values of these quantities as input parameters.

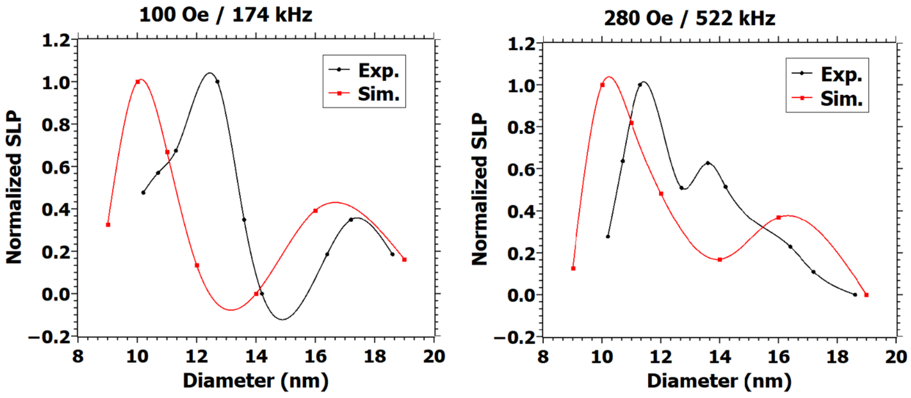

(a) A = 100 Oe and f = 174 kHz **(b)** A = 280 Oe and f = 522 kHz

Figure 4. Comparison between normalized simulated and experimental SLP results for samples of different modal diameters under different field amplitudes and frequencies.

For a monodisperse ensemble of 400 nanoparticles with a diameter of 10 nm and less than 0.1% agglomeration, at 300 K under an external magnetic field of 310 Oe and a frequency of 100 kHz, with an anisotropy constant of K = 3.69 kJ/m^3, a simple change in the saturation magnetization (M_s) from the experimentally measured value of 311 kA/m to the bulk magnetite value of 477 kA/m, and further to the bulk $MnFe_2O_4$ value of 500 kA/m, increases the simulated specific loss power (SLP) by 63 and 58%, respectively.

Considering that magnetic nanoparticles (MNPs) exhibit core−shell nanostructures, probably due to a surface passivation process during nanoparticle synthesis, as observed by Verde et al.,[57] it is reasonable to assume that the nanoparticle's core is predominantly composed of bulk crystalline material. In this case, the core's contribution to the SLP is better described by using the bulk M_s value rather than the experimental one. This observation explains why SLP simulations that consider bulk M_s values show better agreement with the experimental results.

Similarly, for M_s = 477 kA/m, keeping all other parameters constant, but increasing K from 3.69 to 36.90 kJ/m^3 and then further to 369.00 kJ/m^3, results in increases in the simulated SLP values of 9 and 5%, respectively.

The sensitivity of SLP to the choice of saturation magnetization (M_s) and anisotropy constant (K) partially explains why our simulated values are systematically smaller than those of the experimental SLP data. Since the aim of this work is not to determine the parameters that maximize the SLP but rather to test whether our implementation can adequately replicate the experimental data, a direct comparison of absolute values is not the central focus. Instead, we emphasize reproducing the overall behavior and curve profiles.

Another important issue when comparing experimental and simulated data is related to the sample size. While experimental data often make use of samples with thousands of nanoparticles, simulations are normally restricted to hundreds of nanoparticles. In this sense, it is expected that the simulated and theoretical values possess similar magnitudes but not necessarily exact agreement due to the intrinsic limitations of the constructed model. These limitations also include other intrinsic characteristics of our model, such as the random distribution of easy axes in each step and the inherent statistical variations in models based on Monte Carlo simulations due to their stochastic nature. In order to overcome this issue, we have followed an approach where the normalized values of SLP can be directed to be compared. Details of the normalization approach can be found in Supporting Information, S2, Section Normalization framework.

Following this normalization framework, we were able to directly compare the calculated Specific Loss Power (SLP) with the experimental SLP for various external magnetic field amplitudes and frequencies, as shown in Figure 4. As expected, the numerical values and peak positions are not the same. The difference in peak positions, for example, might be attributed to the fact that we do not consider cluster formation in our calculations, since Ruta et al.[25] have suggested that the position of the maximum is related to the packing fraction. However, Ruta et al.[25] indicates that this is the case only for M_s = 400 kA/m, while for M_s = 200 kA/m their data suggest that the dipolar interactions are weak and SLP does not depend on packing fraction. In addition, Papadopoulos et al.[26] data indicate that the anisotropy constant also influences peak positions. Since we have not varied M_s and K, but consider them as constant input values, these kinds of differences are expected. Curve profiles in Figures 4, S4 and S5 reveal that, in general, the simulations are in consonance with the experimental trends: SLP increases with particle diameter until reaching a maximum, after which it decreases. A secondary maximum is observed for larger particle diameters. Notably, the simulated SLP maxima consistently occur at particle diameters that are approximately 20% (or less) smaller than the experimental SLP maxima. Similar results were obtained for different external magnetic fields and frequencies, as clearly seen in the Supporting Information Figures S4 and S5. In addition, our data (see Figure S6 in the Supporting Information) indicate that our simulated results are consistent with the experimental data across a wide range of particle concentrations. A similar trend was observed by Rodrigo et al.[54] using a Stoner−Wohlfarth model. Specifically, for different samples and varying external field amplitudes and frequencies, SLP values tend to increase with the particle diameter up to a maximum value, after which they decrease. However, Rodrigo et al.[54] reported the maximum SLP at a diameter of approximately 20 nm, whereas we observed it at 10 nm. This discrepancy is likely due to differences in the system input parameters such as M_s, K, magnetic field amplitude, and frequency.

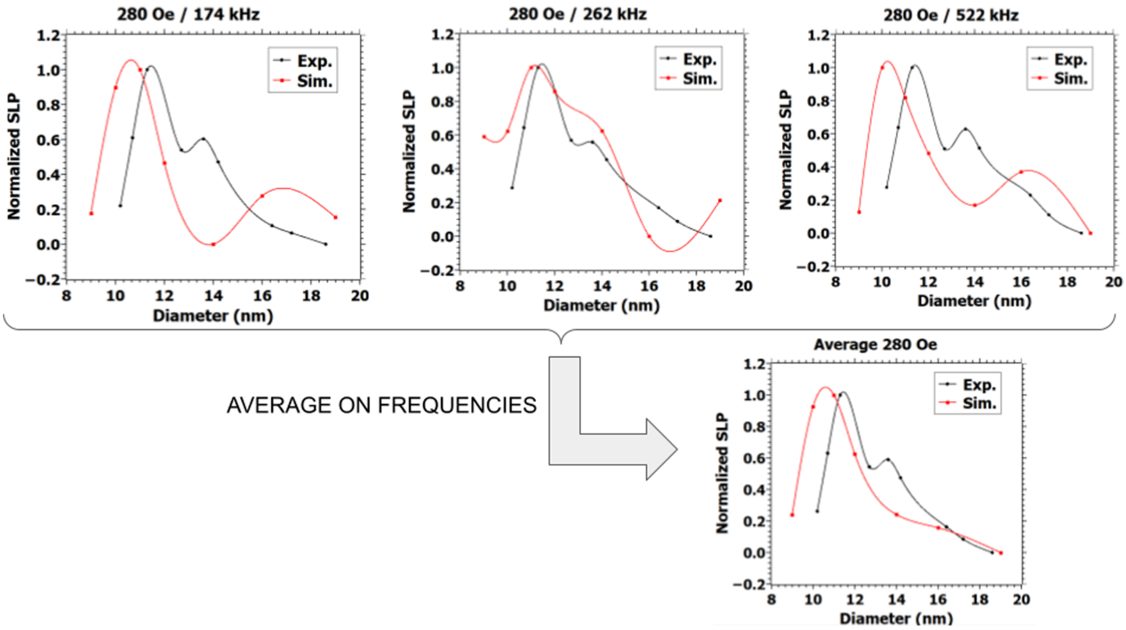

Figure 5. Comparison between normalized simulated and experimental SLP results for samples of different modal diameters under an external magnetic field of 280 Oe and different oscillation frequencies.

The calculated specific loss power (SLP) is primarily correlated to the external magnetic field, particularly its frequency and amplitude. To examine this dependency, averages were computed across different frequencies with the same amplitude. Figure 5 illustrates the averaging process for experimental and simulated results, considering an external magnetic field with an amplitude of 260 Oe and varying frequencies. This procedure notably enhances the agreement between experimental and simulated outcomes, in a clear indication that our implementation is capable of adequately replicating the experimental behavior.

To test the predictive capability of our model, we further explored the use of averages to establish a direct relation between simulated and experimental SLP. First, we estimated the ratio between the maximum values of SLP for different combinations of magnetic field amplitudes and frequencies. Then, we computed the average for each frequency, as described in SI-S4, Experimental and Simulated SLP Comparison. The resulting averages can be correlated with the magnetic field amplitude (see Figure SI-S7), allowing for the determination of SLP values under different conditions and their direct comparison with experimental SLP values at least for the magnetic field amplitudes and frequencies considered by us. Table SI-S1 presents the experimental and simulated SLP values obtained following this scheme.

The average ratio (for each frequency) between the experimental and simulated SLP maximum values shows a clear correlation with magnetic field amplitudes, as illustrated in Figure SI-S7. Using the quadratic fit indicated in Figure SI-S7 ($P_{\gamma}^{\mathrm{avg}} = 1.0943 - 0.0168 \times A + 0.0002 \times A^2$), we generated theoretical predictions for the scenario of frequency f = 740 kHz with amplitudes of A = 100, 130, 160, and 190 Oe. The results are displayed in Table SI-S2 and shown in Figure 6. Based on these results, we can infer that the derived function is transferable, at least for the magnetic field amplitudes and frequencies considered by us, allowing for the prediction of experimental outcomes with an average error of less than 10%.

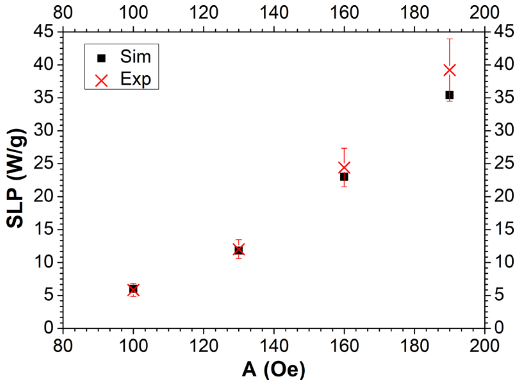

Figure 6. Comparison of experimental and simulated results for a frequency of 740 kHz and different magnetic field amplitudes.

It follows from our overall discussion that our implementation can be used as a tool for evaluating the overall behavior and prediction of the magnetic dynamics of a given set of nanoparticles, at least for the magnetic field amplitudes and frequencies considered in our work. If experimental data are available, it is possible to correlate simulated and experimental SLP data and hence use our computational approach to estimate the actual SLP value in different conditions.

However, it is important to point out that although a system dependent calibration curve is feasible, the deviations observed for simulated and experimental SLP values might arise from the limitations of our implementation, as previously discussed.

■ CONCLUSIONS

In this study, we compare experimental data to a model designed to simulate the magnetic dynamics of magnetic fluids. $MnFe_2O_4$ nanoparticles of distinct sizes, ranging from 10 to 20 nm, were synthesized by hydrothermal method using different bases and the ionic force phase separation process. The nanoparticles were characterized using transmission electron microscopy (TEM), X-ray diffraction (XRD), dynamic light scattering (DLS), and vibrating sample magnetometry. Magnetic hyperthermia properties were evaluated using the calorimetric method as a function of frequency and field amplitude. Magnetic hyperthermia measurements indicate that the specific loss power (SLP) increases with particle diameter up to a certain point after which it begins to decrease. This trend was observed across a wide range of particle concentrations under varying external magnetic field amplitudes and frequencies.

The experimental data were directly compared to our simulation results. These comparisons focused on investigating the dependence of SLP on external magnetic field parameters (amplitude and frequency) as well as the modal diameters of various magnetic fluid samples. Although the numerical values differ slightly due to limitations in our model, the simulated results capture the key characteristics of the experimental data. Furthermore, we demonstrated a strong correlation between the simulated and experimental SLP results, showing good overall agreement.

Therefore, it is fair to say that the proposed kinetic Monte Carlo implementation can be used as a tool for the evaluation and prediction of magnetic dynamics and hence SLP for a given set of nanoparticles, at least for the magnetic field amplitudes and frequencies considered in our work. In other words, our simulation scheme can be used to predict and compare the energy released by different magnetic nanoparticle systems upon being subjected to various external magnetic fields. This capability will aid in the design and development of new magnetic nanoparticles for use in magnetic hyperthermia, allowing for the testing and comparison of new MNPs even before their synthesis.

■ ASSOCIATED CONTENT

Supporting Information

The Supporting Information is available free of charge at https://pubs.acs.org/doi/10.1021/acs.jpcc.4c07127.

> TEM and XRD data; magnetic hyperthermia data; magnetic fluid initial conditions; comparison between normalized and experimental SLP results; simulation and experimental SLP results; and kinetic Monte Carlo details and data (PDF)

■ AUTHOR INFORMATION

Corresponding Author

R. Miotto − *Centro de Cîencias Naturais e Humanas, Universidade Federal do ABC, CEP 09210-580 Santo André, SP, Brazil;* orcid.org/0000-0001-5837-2569; Email: ronei.miotto@ufabc.edu.br

Authors

C. M. Aono − *Centro de Cîencias Naturais e Humanas, Universidade Federal do ABC, CEP 09210-580 Santo André, SP, Brazil*

V. R. R. Aquino − *Instituto de Física, Universidade Federal de Goiás, CEP 74690-900 Goiânia, GO, Brazil*

A. F. Bakuzis − *Instituto de Física, Universidade Federal de Goiás, CEP 74690-900 Goiânia, GO, Brazil; CNanoMed, Universidade Federal de Goiás, Goiânia, GO 74690-631, Brazil;* orcid.org/0000-0003-3366-106X

Complete contact information is available at: https://pubs.acs.org/10.1021/acs.jpcc.4c07127

Funding

The Article Processing Charge for the publication of this research was funded by the Coordination for the Improvement of Higher Education Personnel - CAPES (ROR identifier: 00x0ma614).

Notes

The authors declare no competing financial interest.

■ ACKNOWLEDGMENTS

The authors thank Capes for financial support.

■ REFERENCES

(1) Wagner, V.; Dullaart, A.; Bock, A. K.; Zweck, A. The emerging nanomedicine landscape. *Nat. Biotechnol.* **2006**, *24*, 1211−1217.

(2) Michael, E.; Evans, F. H. *Environmental Magnetism Principles and Applications of Enviromagnetics*, 1st ed.; Academic Press: 2003; p 299.

(3) Sellmyer, D.; Skomski, R. In *Advanced Magnetic Nanostructures*; Sellmyer, D.; Skomski, R., Eds.; Springer US: Boston, MA, 2006; pp 1−508.

(4) Ulbrich, K.; Holá, K.; Šubr, V.; Bakandritsos, A.; Tuček, J.; Zbořil, R. Targeted Drug Delivery with Polymers and Magnetic Nanoparticles: Covalent and Noncovalent Approaches, Release Control, and Clinical Studies. *Chem. Rev.* **2016**, *116*, 5338−5431.

(5) Tietze, R.; Zaloga, J.; Unterweger, H.; Lyer, S.; Friedrich, R. P.; Janko, C.; Pöttler, M.; Dürr, S.; Alexiou, C. Magnetic nanoparticle-based drug delivery for cancer therapy. *Biochem. Biophys. Res. Commun.* **2015**, *468*, 463−470.

(6) Aires, A.; Ocampo, S. M.; Simões, B. M.; Josefa Rodríguez, M.; Cadenas, J. F.; Couleaud, P.; Spence, K.; Latorre, A.; Miranda, R.; Somoza, A.; et al. Multifunctionalized iron oxide nanoparticles for selective drug delivery to CD44-positive cancer cells. *Nanotechnology* **2016**, *27*, No. 065103.

(7) Lim, B. K.; Tighe, E. C.; Kong, S. D. The use of magnetic targeting for drug delivery into cardiac myocytes. *J. Magn. Magn. Mater.* **2019**, *473*, 21−25.

(8) Leong, S. S.; Yeap, S. P.; Lim, J. Working principle and application of magnetic separation for biomedical diagnostic at high- and low-field gradients. *Interface Focus* **2016**, *6*, 20160048.

(9) Zhou, Z.; Yang, L.; Gao, J.; Chen, X. Structure−Relaxivity Relationships of Magnetic Nanoparticles for Magnetic Resonance Imaging. *Adv. Mater.* **2019**, *31*, No. 1804567.

(10) Rocha, J. V. R.; Krause, R. F.; Ribeiro, C. E.; Oliveira, N. C. D. A.; Ribeiro De Sousa, L.; Leandro Santos, J.; Castro, S. D. M.; Valadares, M. C.; Cunha Xavier Pinto, M.; Pavam, M. V.et al.Near Infrared Biomimetic Hybrid Magnetic Nanocarrier for MRI-Guided Thermal Therapy. *ACS Appl. Mater. Interfaces* **2024**,

(11) Bauer, L. M.; Situ, S. F.; Griswold, M. A.; Samia, A. C. S. Magnetic Particle Imaging Tracers: State-of-the-Art and Future Directions. *J. Phys. Chem. Lett.* **2015**, *6*, 2509−2517.

(12) Cabrera, D.; Coene, A.; Leliaert, J.; Artés-Ibáñez, E. J.; Dupré, L.; Telling, N. D.; Teran, F. J. Dynamical Magnetic Response of Iron Oxide Nanoparticles Inside Live Cells. *ACS Nano* **2018**, *12*, 2741−2752.

(13) Rodrigues, H. F.; Capistrano, G.; Bakuzis, A. F. In vivo magnetic nanoparticle hyperthermia: a review on preclinical studies, low-field nano-heaters, noninvasive thermometry and computer simulations for treatment planning. *International Journal of Hyperthermia* **2020**, *37*, 76−99.

(14) Deatsch, A. E.; Evans, B. A. Heating efficiency in magnetic nanoparticle hyperthermia. *J. Magn. Magn. Mater.* **2014**, *354*, 163−172.

(15) Yang, Z.; Gao, D.; Zhao, J.; Yang, G.; Guo, M.; Wang, Y.; Ren, X.; Kim, J. S.; Jin, L.; Tian, Z.; et al. Thermal immuno-nanomedicine in cancer. *Nature Reviews Clinical Oncology* **2023**, *20*, 116−134.

(16) Gilchrist, R. K.; Medal, R.; Shorey, W. D.; Hanselman, R. C.; Parrott, J. C.; Taylor, C. B. Selective inductive heating of lymph nodes. *Annals of surgery* **1957**, *146*, 596−606.

(17) Spirou, S.; Basini, M.; Lascialfari, A.; Sangregorio, C.; Innocenti, C. Magnetic Hyperthermia and Radiation Therapy: Radiobiological Principles and Current Practice †. *Nanomaterials* **2018**, *8*, 401.

(18) PéRigo, E. A.; Hemery, G.; Sandre, O.; Ortega, D.; Garaio, E.; Plazaola, F.; Teran, F. J. Fundamentals and advances in magnetic hyperthermia. *Applied Physics Reviews* **2015**, *2*, No. 041302.

(19) Angelakeris, M. Magnetic nanoparticles: A multifunctional vehicle for modern theranostics. *Biochimica et Biophysica Acta (BBA) - General Subjects* **2017**, *1861*, 1642−1651.

(20) Chang, D.; Lim, M.; Goos, J. A. C. M.; Qiao, R.; Ng, Y. Y.; Mansfeld, F. M.; Jackson, M.; Davis, T. P.; Kavallaris, M. Biologically Targeted Magnetic Hyperthermia: Potential and Limitations. *Front. Pharmacol.* **2018**, *9*, 831.

(21) Mahmoudi, K.; Bouras, A.; Bozec, D.; Ivkov, R.; Hadjipanayis, C. Magnetic hyperthermia therapy for the treatment of glioblastoma: a review of the therapy's history, efficacy and application in humans. *International Journal of Hyperthermia* **2018**, *34*, 1316−1328.

(22) Maier-Hauff, K.; Ulrich, F.; Nestler, D.; Niehoff, H.; Wust, P.; Thiesen, B.; Orawa, H.; Budach, V.; Jordan, A. Efficacy and safety of intratumoral thermotherapy using magnetic iron-oxide nanoparticles combined with external beam radiotherapy on patients with recurrent glioblastoma multiforme. *Journal of Neuro-Oncology* **2011**, *103*, 317−324.

(23) Carrey, J.; Mehdaoui, B.; Respaud, M. Simple models for dynamic hysteresis loop calculations of magnetic single-domain nanoparticles: Application to magnetic hyperthermia optimization. *J. Appl. Phys.* **2011**, *109*, No. 083921.

(24) Tan, R. P.; Carrey, J.; Respaud, M. Magnetic hyperthermia properties of nanoparticles inside lysosomes using kinetic Monte Carlo simulations: Influence of key parameters and dipolar interactions, and evidence for strong spatial variation of heating power. *Phys. Rev. B* **2014**, *90*, No. 214421.

(25) Ruta, S.; Chantrell, R.; Hovorka, O. Unified model of hyperthermia via hysteresis heating in systems of interacting magnetic nanoparticles. *Sci. Rep.* **2015**, *5*, 9090.

(26) Papadopoulos, C.; Kolokithas-Ntoukas, A.; Moreno, R.; Fuentes, D.; Loudos, G.; Loukopoulos, V. C.; Kagadis, G. C. Using kinetic Monte Carlo simulations to design efficient magnetic nanoparticles for clinical hyperthermia. *Medical Physics* **2022**, *49*, 547−567.

(27) Capistrano, G.; Rodrigues, H. F.; Zufelato, N.; Gonçalves, C.; Cardoso, C. G.; Silveira-Lacerda, E. P.; Bakuzis, A. F. Noninvasive intratumoral thermal dose determination during in vivo magnetic nanoparticle hyperthermia: combining surface temperature measurements and computer simulations. *International Journal of Hyperthermia* **2020**, *37*, 120−140.

(28) Peters, J. A. Relaxivity of manganese ferrite nanoparticles. *Prog. Nucl. Magn. Reson. Spectrosc.* **2020**, *120−121*, 72−94.

(29) Prospero, A. G.; Buranello, L. P.; Fernandes, C. A.; dos Santos, L. D.; Soares, G.; C Rossini, B.; Zufelato, N.; Bakuzis, A. F.; De Mattos Fontes, M. R.; De Arruda Miranda, J. R. Corona Protein Impacts on Alternating Current Biosusceptometry Signal and Circulation Times of Differently Coated Mnfe 2 O 4 Nanoparticles. *Nanomedicine* **2021**, *16*, 2189−2206.

(30) Aquino, V. R. R.; Vinícius-Araújo, M.; Shrivastava, N.; Sousa, M. H.; Coaquira, J. A. H.; Bakuzis, A. F. Role of the Fraction of Blocked Nanoparticles on the Hyperthermia Efficiency of Mn-Based Ferrites at Clinically Relevant Conditions. *J. Phys. Chem. C* **2019**, *123*, 27725−27734.

(31) Zufelato, N.; Aquino, V. R. R.; Shrivastava, N.; Mendanha, S.; Miotto, R.; Bakuzis, A. F. Heat Generation in Magnetic Hyperthermia by Manganese Ferrite-Based Nanoparticles Arises from Néel Collective Magnetic Relaxation. *ACS Applied Nano Materials* **2022**, *5*, 7521−7539.

(32) Massart, R.; Dubois, E.; Cabuil, V.; Hasmonay, E. Preparation and properties of monodisperse magnetic fluids. *J. Magn. Magn. Mater.* **1995**, *149*, 1−5.

(33) Hergt, R.; Dutz, S.; Röder, M. Effects of size distribution on hysteresis losses of magnetic nanoparticles for hyperthermia. *J. Phys.: Condens. Matter* **2008**, *20*, No. 385214.

(34) Shaterabadi, Z.; Nabiyouni, G.; Soleymani, M. Physics responsible for heating efficiency and self-controlled temperature rise of magnetic nanoparticles in magnetic hyperthermia therapy. *Prog. Biophys. Mol. Biol.* **2018**, *133*, 9−19.

(35) Verde, E. L.; Landi, G. T.; Gomes, J. A.; Sousa, M. H.; Bakuzis, A. F. Magnetic hyperthermia investigation of cobalt ferrite nanoparticles: Comparison between experiment, linear response theory, and dynamic hysteresis simulations. *J. Appl. Phys.* **2012**, *111*, 123902.

(36) Rosensweig, R. E. Heating magnetic fluid with alternating magnetic field. *J. Magn. Magn. Mater.* **2002**, *252*, 370−374.

(37) Coffey, W. T.; Kalmykov, Y. P. Thermal fluctuations of magnetic nanoparticles: Fifty years after Brown. *J. Appl. Phys.* **2012**, *112*, 121301.

(38) Stoner, E. C.; Wohlfarth, E. P. A mechanism of hysteresis in heterogeneous alloys. *Philos. Trans. R. Soc., A* **1948**, *240*, 599.

(39) Guimarães, A. P. *Principles of Nanomagnetism*, 1st ed.; NanoScience and Technology; Springer Berlin Heidelberg: Berlin, Heidelberg, 2009; p 221.

(40) Klik, I.; Chang, C.; Lee, J. Master equation approach to anhysteresis of noninteracting particles. *J. Appl. Phys.* **1994**, *75*, 5487−5489.

(41) Chantrell, R. W.; Walmsley, N.; Gore, J.; Maylin, M. Calculations of the susceptibility of interacting superparamagnetic particles. *Phys. Rev. B* **2000**, *63*, No. 024410.

(42) Dormann, J. L.; Fiorani, D.; Tronc, E. In *Advances in Chemical Physics, Vol. 98*; Prigogine, I.; Rice, S. A., Eds.; John Wiley & Sons, Inc.: 1997; pp 283−494.

(43) Néel, L. Théorie du traînage magnétique des substances massives dans le domaine de Rayleigh. *Journal de Physique et le Radium* **1950**, *11*, 49−61.

(44) Brown, W. F. Thermal Fluctuations of a Single-Domain Particle. *Phys. Rev.* **1963**, *130*, 1677−1686.

(45) Guimarães, A. P.; Oliveira, I. S. *Magnetism and Magnetic Resonance in Solids*; Wiley-Interscience: 1998; p 297.

(46) Kodama, R. Magnetic nanoparticles. *J. Magn. Magn. Mater.* **1999**, *200*, 359−372.

(47) Garanin, D. A.; Kachkachi, H. Surface Contribution to the Anisotropy of Magnetic Nanoparticles. *Phys. Rev. Lett.* **2003**, *90*, No. 065504.

(48) Chudnovsky, E. M.; Tejada, J. *Macroscopic Quantum Tunneling of the Magnetic Moment*; Cambridge University Press: Cambridge, 1998; p 173.

(49) Kachkachi, H.; Bonet, E. Surface-induced cubic anisotropy in nanomagnets. *Phys. Rev. B* **2006**, *73*, No. 224402.

(50) Newman, M. E. J.; Barkema, G. T. *Monte Carlo Methods in Statistical Physics*; Oxford University Press: Oxford, 1999; p 490.

(51) Kirkpatrick, S.; Gelatt, C. D.; Vecchi, M. P. Optimization by Simulated Annealing. *Science* **1983**, *220*, 671−680.

(52) Castro, L.; Gonçalves, G.; Neto, K.; Morais, P.; Bakuzis, A.; Miotto, R. Role of surfactant molecules in magnetic fluid: Comparison of Monte Carlo simulation and electron magnetic resonance. *Phys. Rev. E* **2008**, *78*, No. 061507.

(53) Bakuzis, A. F.; Branquinho, L. C.; Luize Castro, L.; De Amarale Eloi, M. T.; Miotto, R. Chain formation and aging process in biocompatible polydisperse ferrofluids: Experimental investigation and Monte Carlo simulations. *Adv. Colloid Interface Sci.* **2013**, *191−192*, 1−21.

(54) Rodrigo, I.; Castellanos-Rubio, I.; Garaio, E.; Arriortua, O. K.; Insausti, M.; Orue, I.; García, J. Á.; Plazaola, F. Exploring the potential of the dynamic hysteresis loops via high field, high frequency and temperature adjustable AC magnetometer for magnetic hyperthermia characterization. *International Journal of Hyperthermia* **2020**, *37*, 976−991.

(55) Ring, H. L.; Sharma, A.; Ivkov, R.; Bischof, J. C. The impact of data selection and fitting on SAR estimation for magnetic nanoparticle heating. *International Journal of Hyperthermia* **2020**, *37*, 100−107.

(56) Aquino, V. R. R. *A influência da anisotropia, diâmetro e interação dipolar na hipertermia magnética de nanoferritas Mn x A 1-x Fe2O4: relaxação coletiva e a fração de nanopartículas responsáveis pela geração de calor*, Ph.D. thesis; Universidade Federal de Goias: 2018.

(57) Verde, E. L.; Landi, G. T.; Carrião, M. S.; Drummond, A. L.; Gomes, J. A.; Vieira, E. D.; Sousa, M. H.; Bakuzis, A. F. Field dependent transition to the non-linear regime in magnetic hyperthermia experiments: Comparison between maghemite, copper, zinc, nickel and cobalt ferrite nanoparticles of similar sizes. *AIP Adv.* **2012**, *2*, No. 032120.